Comparative Research on Four-Phase Dual Armature-Winding Wound-Field Doubly Salient Generator With Distributed Field Magnetomotive Forces for High-Reliability Application

YAO ZHAO[1], **DENGHUI TENG**[1], **DONGDONG LI**[1], (Member, IEEE), **AND XING ZHAO**[2], (Member, IEEE)

[1]College of Electric Power Engineering, Shanghai University of Electric Power, Shanghai 200090, China
[2]Department of Electrical Engineering, The Hong Kong Polytechnic University, Hong Kong, China

Corresponding author: Dongdong Li (powerldd@163.com)

ABSTRACT In this article, a four-phase dual armature-winding wound-field doubly salient machine with distributed field magnetomotive forces (DAW-WFDSM-DF) and corresponding double-redundant rectifier circuit are proposed to improve the electromagnetic performance of the traditional WFDSM in terms of the output voltage ripple, fault-tolerant capability and output capability. Firstly, due to the uniformly distributed field magnetomotive forces of the proposed machine, the more feasible stator/rotor pole combinations of the four-phase machine can be obtained and the influence of stator/rotor-pole combination on electromagnetic performance is investigated, especially for the fault-tolerant capability. Based on a multi-objective evaluation function including output capability, fault-tolerant capability and unbalanced magnetic forces, the $4N$-stator-pole/$3N$-rotor-pole ($4N/3N$) and $4N/5N$ combinations are recommended. Then, considering that the fault-tolerant capability of 8/6-pole machine is poorer than that of 12/9-pole one, the 12/9-pole and 8/10-pole DAW-WFDSM-DFs are comparatively researched for taking as the representatives of $4N/3N$ and $4N/5N$, including no-load and on-load characteristics and fault-tolerance performance under single winding open-circuit condition. Finally, as the 8/10-pole DAW-WFDSM-DF exhibits remarkably higher efficiency and stronger fault-tolerant capability than the 12/9-pole one, an 8/10-pole prototype is manufactured and tested to verify the analytical results.

INDEX TERMS Fault-tolerant capability, stator/rotor pole combination, dual armature-winding, wound field doubly salient generator, distributed field magnetomotive forces, electromagnetic performance.

I. INTRODUCTION

Due to their simple rotor structure, stator-excited machines have attracted increasing research interest over the last decade and are recognized as suitable for airplane and electric vehicle applications [1]–[4]. Generally, there are three types of stator-excited machines that have magnets or field windings located on the stator: 1) a stator permanent magnet (PM) machine; 2) a stator hybrid excitation machine; and 3) a stator wound-field machine. As a representative stator-excited machine, a reluctance machine with a salient stator and rotor pole is presented.

Apart from inheriting the stator-PM doubly salient machines (PMDSMs) with merits of simple structure, the absence of retaining sleeve and excellent rotor thermal dissipation, a certain flux-regulation capability of hybrid excitation doubly salient machines (HEDSMs) can be achieved to improve the flux-weakening capability, resulting in improved efficiency over a wide speed range [5]–[8]. However, PMs still exist, and an irreversible demagnetization risk also exists in the HEDSMs and PMDSMs, resulting in restricted fields of application for the HEDSMs and PMDSMs.

The associate editor coordinating the review of this manuscript and approving it for publication was Yonghao Gui.

Based on these disadvantages, PM-free machines, i.e., switched reluctance machines (SRMs) and wound-field doubly salient machines (WFDSMs), have attracted research interest due to their simple and robust structure and fault-tolerance capability. Compared to the SRMs, the low noise and vibration levels of WFDSMs are obtained from the smooth output torque; In addition, controlled converter devices and rotor position sensors are not needed, and the reliability is thus improved [9], [10].

For WFDSMs, the magnetic field is controllable by regulating the field current. Moreover, the advantages of robust structure and the absence of PMs make them suitable as an auxiliary power unit generator and as an aircraft starter-generator [10].

The current research on WFDSMs is mainly divided into three areas: topology design, starter/generator (S/G) and position sensorless control [10]–[19]. In [11], a two-section twisted-rotor structure for WFDSM was proposed to decrease output voltage ripple significantly. In [12], dual dual armature-winding WFDSM (DAW-WFDSM) with hybrid half-wave rectifiers (HHWRs) were comparatively researched with traditional WFDSM with full-bridge rectifiers and half-bridge rectifiers to obtain low output voltage ripple. In [13], a novel five-phase brushless DESM with symmetrical phase was presented to address the phase asymmetry shortcoming and improve the fault-tolerance capability due to a multiphase armature winding. In [14], a novel WFDSM with split-field winding was investigated to reduce the capacity of the field current regulator. In terms of S/G voltage, copper loss optimization based on a bidirectional converter is proposed to reduce the copper loss and the weight of the inverter/rectifier unit [15]. In [16], an indirect adaptive fuzzy control for reducing the output voltage ripple was investigated. In [17], A novel control method with field current inner loop and speed outer loop for WFDSM is proposed to improve system driving efficiency and reduce the torque ripple. In [18], the negative-going zero-crossing points of the line-to-line field flux linkage were utilized for the detection of the position and speed of the rotor. In [19], based on a self-inductance rectangle, a highly accurate position senseless control strategy without negative torque was proposed.

In general, a WFDSM is more suitable for power generation applications, such as aerospace generator and electric vehicle (EV) generator. However, since the field winding spans m stator poles (m is phase number) to form N-pole or S-pole, the flux path of each phase of the WFDSM is asymmetry, resulting in high output voltage ripple and torque ripple. In order to the overcome these drawbacks, the WFDSM with distributed field magnetomotive forces (WFDSM-DF), which is characterized by the dc-field winding equipped in each stator pole, is introduced and developed [20]. With the aid of uniformly distributed dc-field winding, the flux path of each phase is symmetrical and more feasible stator/rotor pole combinations are obtained. In addition, in order to make the WFDSM-DF suitable for high-reliability

applications, the proposed machine integrating the four-phase structure and the dual armature winding structure equipped with double-redundant rectifier circuit has the potential to improve fault-tolerant capability. In fact, aerospace/EV application demand high reliability, high availability, and high power density while aiming to reduce weight, volume and operational costs. For four-phase machine, the stronger fault-tolerant capability can be obtained compared to the three-phase one, and the higher power density can be obtained compared to the five-phase one. Thus, the choice of four-phase one will be considered as a compromise between fault-tolerant capability and power density [22]. Furthermore, in order to obtain the better fault-tolerant capability, the influence of stator/rotor pole combination on the fault-tolerant capability is also investigated. In addition, for the different stator/rotor pole combinations of the DAW-WFDSM-DF with double-redundant rectifier circuit, comprehensive comparisons are made to select the optimum configuration.

This article is organized as follows. In section II, the feasible stator/rotor pole combinations of four-phase WFDSM-DFs and the influence stator/rotor pole combinations on output capability, fault-tolerant capability and unbalanced magnetic force are presented. Additionally, the operational principle of a dual armature-winding WFDSM-DF (DAW-WFDSM-DF) with double-redundant rectifier circuit is introduced in detail based on simplified phase vector diagrams. In section III, taking 8/10-pole and 12/9-pole DAW-WFDSM-DFs as the representatives of the 4N/5N and 4N/3N structures, the no-load, on-load characteristics and fault-tolerant capability are comprehensively compared. In section IV, an 8/10-pole DAW-WFDSM-DF prototype is manufactured to validate finite element analyses. Finally, conclusions are presented in section V.

II. STATOR/ROTOR POLE COMBINATIONS AND OPERATION PRINCIPLE OF FOUR-PHASE WFDSM-DF
A. FEASIBLE STATOR AND ROTOR POLE COMBINATIONS
For a traditional WFDSM, the stator/rotor pole combinations can be expressed as follows [13]:

$$\begin{cases} \dfrac{N_s}{N_r} = \dfrac{m}{m \pm 1} \\ \dfrac{N_s}{m} = 2k \end{cases} \tag{1}$$

where N_s and N_r are the stator pole number and the rotor pole number, respectively. m is the phase number, and k is a positive integer. The m stator poles are covered by one set of field windings, and the number of slots for field windings must be an even number. Therefore, in four-phase WFDSM, the stator pole number is 4, 8, 16, 24 and so on.

Due to uniformly distributed dc-field winding of WFDS-M-DF, more feasible stator/rotor pole combinations can be obtained to realize better electromagnetic performance. The feasible stator/rotor pole combinations for a WFDSM-DF can be governed by

$$\frac{N_s}{GCD\{N_s, N_r\}} = km \tag{2}$$

TABLE 1. Feasible Stator/Rotor pole Combinations of Four-Phase WFDSM-DF.

N_s	4	8	12	16	4	8	12	16
	3	3	3	3	13	13	13	13
	-	-	-	4	-	14	-	14
	5	5	5	5	15	15	15	15
	-	6	-	6	-	-	-	-
N_r	7	7	7	7	17	17	17	17
	-	-	-	-	-	18	-	18
	9	9	9	9	19	19	19	19
	-	10	-	10	-	-	-	20
	11	11	11	11	21	21	21	21
	-	-	-	12	-	22	-	22

where $GCD\{N_s, N_r\}$ is the most common divisor of the stator and rotor pole numbers. For the four-phase WFDSM-DF, the feasible stator/rotor pole combinations without any special consideration are shown in Table 1. However, some combinations in Table 1 are not recommendable, i.e., 4/7, 4/9, 12/3, and 12/5. The more rotor pole numbers may cause a significant increase in iron loss, while the fault-tolerant capability is weak with less rotor pole. Therefore, all undesirable combinations based on the reasons mentioned above are eliminated and impaled on a red strikeout line ($\boxtimes$). In addition, considering the design goal of the WFDSM-DF, i.e., maximum power and strong fault-tolerant capability, remaining stator/rotor pole combinations that are not impaled on the red strikeout line need to be further selected, which is investigated by taking 8-stator-pole WFDSM-DFs as examples.

The 8-stator-pole WFDSM-DFs with 6, 7, 9, 10, and 11 rotor poles are shown in Fig. 1. Furthermore, for the sake of synthesizing four-phase WFDSM-DFs, the groups of coil EMF vectors for 6, 7, 9, 10, and 11 rotor poles can be determined based on the maximum phase EMF by minimizing the angular displacement, as shown in Fig. 2. The corresponding angular difference θ of coil EMF vectors of the same phase is 45 deg. Obviously, the different groups of coil EMF vectors for 6, 7, 9, 10, and 11 rotor pole machines cause differences in the flux paths interacted by field and armature windings, resulting in differences in the mutual inductance magnitude between field and armature windings and hence influencing the electromagnetic torque magnitude. For the WFDSM, the electromagnetic torque of each phase can be expressed as follows [20]:

$$T_p = T_{pf} + T_{pp} + T_{ff}$$
$$= i_p \cdot i_f \cdot \frac{dL_{pf}}{d\theta} + \frac{1}{2} \cdot i_p^2 \cdot \frac{dL_p}{d\theta} + \frac{1}{2} \cdot i_f^2 \cdot \frac{dL_f}{d\theta} \quad (3)$$

where T_{pf} is the excitation torque excited by the mutual inductance variation between the field winding and armature winding, T_{pp} and T_{ff} are the reluctance torque excited by the self-inductance variation of AC coils only and that of DC coils only, respectively. θ is the electrical angle. i_f and i_p are the field current and phase current, respectively. In general, T_{pf} is much larger than either T_{pp} or T_{ff}. Furthermore, the total
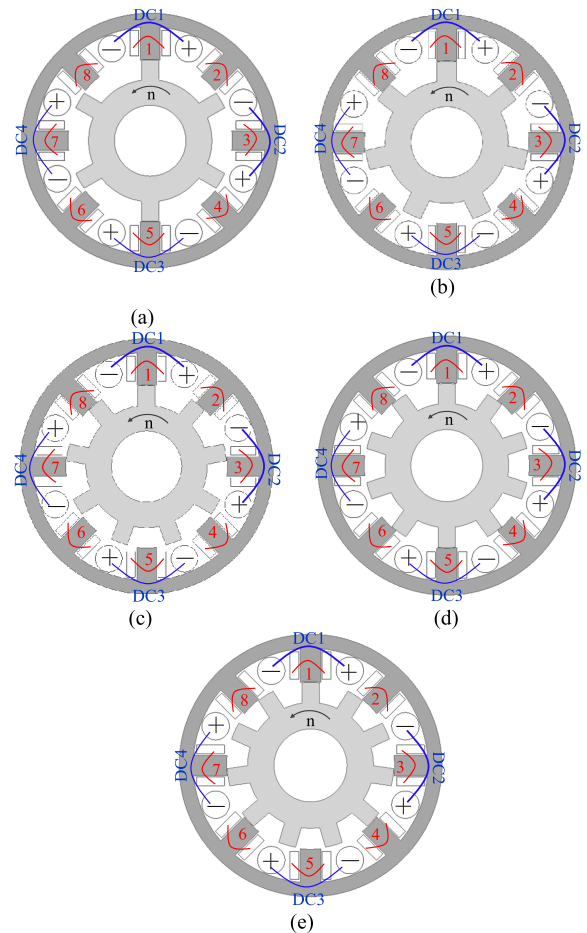

FIGURE 1. Machine topologies in eight-stator-pole WFDSM-DF (a) 8s/6r. (b) 8s/7r. (c) 8s/9r. (d) 8s/10r. (e) 8s/11r.

electromagnetic torque can be expressed as follows:

$$T_e = \sum_{i=1}^{n} T_i \quad (4)$$

where n represents the number of phases that simultaneously produce electromagnetic torque. When neglecting ohmic, iron losses and mechanical loss, T_e is proportional to the output power. The parameters for the 8-stator-pole WFDSM-DF with 6-/7-/9-/10-/11-rotor pole numbers are shown in Table 2. When the rotation speed is 1000 rpm and the full-bridge rectifier is employed, the corresponding T_e versus field current is shown in Fig. 3. Obviously, among these rotor pole number combinations for 8-stator-pole WFDSM-DFs, the 10-rotor-pole machine shows the largest torque density and has the potential to output the maximum power, followed by the 9-/7-/11-/6-rotor-pole machine.

Further, since WFDSMs is widely used in some high-reliability area, the fault-tolerant capability is also considered during investigating stator/rotor pole combination. In generally, the significant requirements for improving fault-tolerant capability should be considered as follows [22]: 1) electrical/magnetic isolation between phases; 2) phase number; 3) effective thermal isolation between phases;
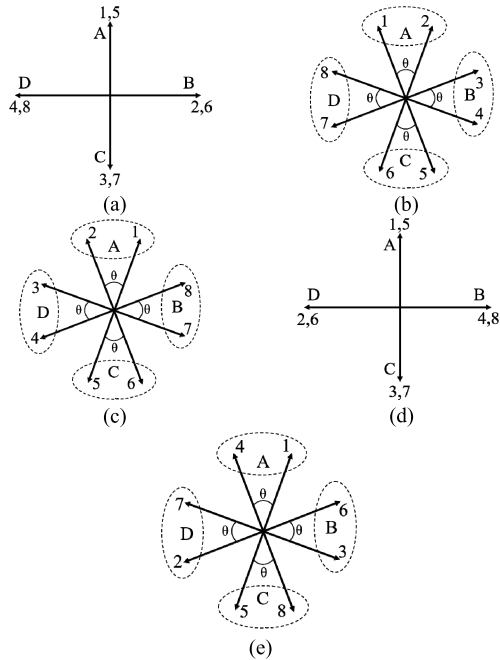
FIGURE 2. Coil EMF vectors in four-stator-pole WFDSM-DF (a) 8s/6r. (b) 8s/7r. (c) 8s/9r. (d) 8s/10r. (e) 8s/11r.

TABLE 2. Parameters for 8-Stator-Pole Four-Phase WFDSM-DF With 6-/7-/9-/10-/11- Rotor Pole Number.

Parameter	Value	
Stator outer diameter, D_0 (mm)	180	
Stack length, L(mm)	90	
Number of turns per coil/ armature windings	40	
Number of turns per coil/ field windings	45	
Stator back-iron height(mm)	13	
Rotor diameter (mm)	115	
Air gap(mm)	0.5	
Stator pole arc/°	14	
Rotor pole arc/°	6-pole	17
	7-pole	15
	9-pole	13
	10-pole	12
	11-pole	12

4) physical isolation between phases; 5) implicit limiting of short-circuit current. Thus, the short-circuit current is reduced by increasing the self-inductance under short-circuit fault and the magnetic coupling effect can be suppressed by decreasing the mutual-inductance between phases, which are significant to improve fault-tolerant capability. To quantitatively express the fault-tolerant capability, the ratio γ of phase self-inductance L_{ii} to mutual-inductance M_{ij} between phases is expressed as [23]

$$\gamma = \frac{L_{ii}}{M_{ij}} \tag{5}$$

Since different stator/rotor pole combinations have effect on arrangement of the armature coils of the same phase and hence influence the inductance characteristic of each phase, the self- and mutual-inductances of 8-stator-pole WFDSM-DF with 6-/7-/9-/10-/11-rotor pole numbers are shown in Fig. 4, taking the self-inductance of phase A and
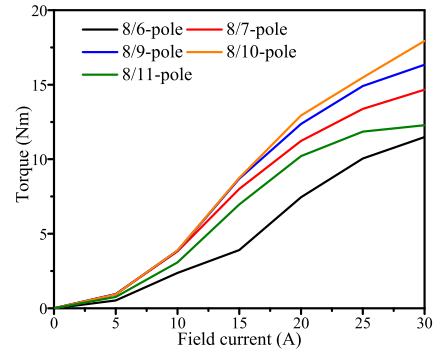

FIGURE 3. Torque versus field current ($n = 1000$ rpm, $R_0 = 0.65\ \Omega$).
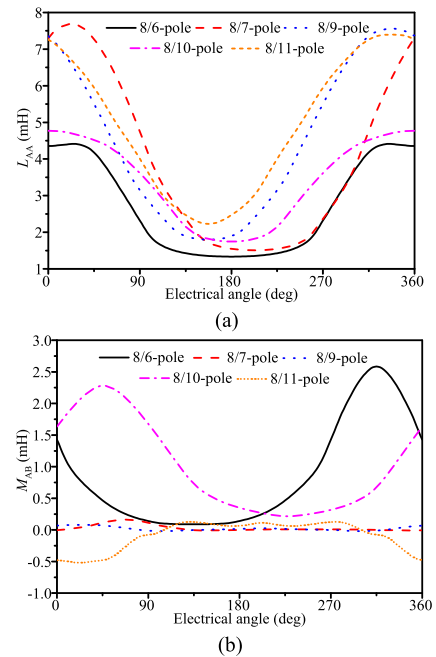

FIGURE 4. The inductance. (a) Self-inductance of phase A. (b) Mutual-inductance between phase A and phase B.

TABLE 3. Self-/Mutual-Inductance and Ratio Γ of the WFDSM-DF.

	8/6-pole	8/7-pole	8/9-pole	8/10-pole	8/11-pole
L_{AA} (mH)	2.67	4.28	4.45	3.36	4.11
M_{AB} (mH)	0.83	0.03	0.02	0.97	-0.08
γ	3.21	142.67	222.5	3.46	51.37

the mutual-inductance between phase A and phase B as examples. The self-/mutual-inductances and corresponding ratio γ are presented in Table 3. The value of self-inductance of 8/9-pole machine is biggest, followed by the 8/7-pole, 8/11-pole, 8/10-pole and 8/6-pole machine. While the value of mutual-inductance of 8/10-pole machine is biggest, followed by the 8/6-pole, 8/11-pole, 8/7-pole and 8/9-pole machine. Especially, the mutual-inductance values of 8/7-pole and 8/9-pole machines are almost zero. The fault-tolerant capability of 8/9-pole machine is strongest, followed
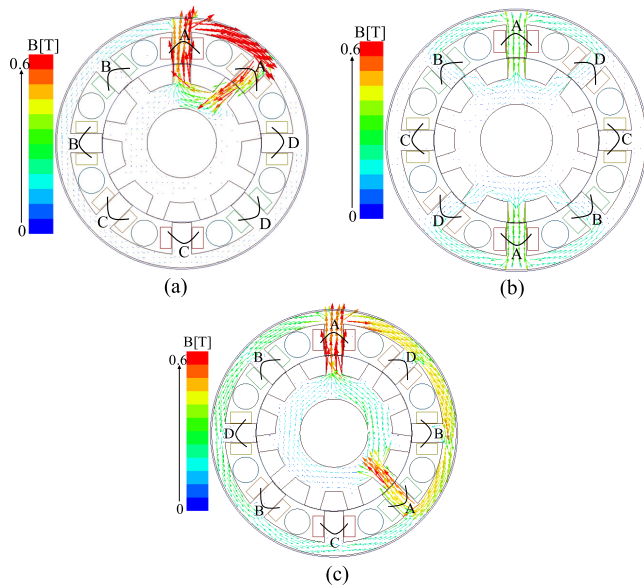
FIGURE 5. The armature reaction flux vector of phase A. (a) 8/9-pole machine. (b) 8/10-pole machine. (c) 8/11-pole machine.

FIGURE 6. UMFs in 7-, 9- and 11-pole machines ($n = 1000$ rpm, $R_0 = 0.65\ \Omega$).

by the 8/7-pole, 8/11-pole, 8/10-pole and 8/6-pole machine. The reason will be illustrated by flux vector distribution by taking 8/9-pole, 8/10-pole and 8/11-pole machines as examples. Fig. 5 shows the A-phase armature flux vector distribution when field current is zero and only phase A is excited as well as the flux linkage of phase A is maximum. For 8/9-pole machine, the flux vector interaction between phase A and phase B is small and negligible, so the mutual-inductance between phase A and phase B is small and negligible. While for the 8/10-pole machine, the flux vector interaction of phase A to adjacent phases is obvious and the mutual-inductance between phases is big. For the 8/11-pole machine, the long flux path of phase A reduces the self-inductance and increases mutual-inductance between phases compared to the 8/9-pole one. In addition, for the 8/9-pole machine, armature winding of phase A is comprised of two coils connected in series on adjacent stator poles. The flux path of phase A is short and thus the self-inductance is big. While for the 8/10-pole machine, since the armature winding of phase A is comprised of two coils connected in series on diametrically stator poles and the flux vector distribution of two coils is not continuous, the flux path of phase A is longer and the airgap length through which the flux linkage passes is triple than that of 8/9-pole machine. Therefore, the self-inductance of 8/10-pole machine is smaller compared to the 8/9-pole one. For 8/11-pole machine, since the flux path is longer than that of 8/9-pole one and shorter than that of 8/10-pole one, the self-inductance of 8/11-pole machine is bigger than that of 8/10-pole one and smaller than that of 8/9-pole one. Consequently, from Table 1, it can be concluded that for the stator/rotor pole combinations with $4N/3N$ and $4N/5N$ and the corresponding distributed factor of 1th EMF harmonic is 1 (the corresponding coil EMF vectors diagrams are similar to Fig. 2(a)), the fault-tolerant
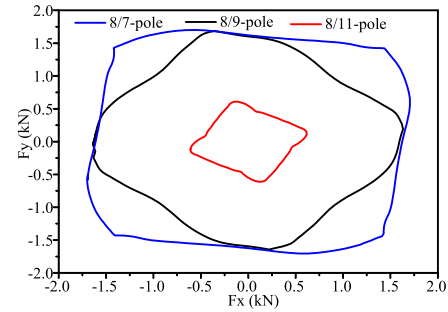
capability is weak compared to the other stator/rotor pole combinations whose the corresponding distributed factor of 1th EMF harmonic is 0.923 and the coil EMF vector diagrams are similar to Fig. 2(c).

However, as shown in Fig. 6, unbalanced magnetic forces (UMFs) exist in 7-/9-/11-rotor-pole machines due to the diametrically asymmetric windings [21], e.g., the flux path interacted by field windings and different armature winding coils of the same phase (see Fig. 2) is asymmetric, resulting in circumferentially asymmetric magnetic density in the air gap. Vibration and noise can be incurred due to UMFs, which is harmful to the onboard load. Thus, the desirable rotor pole numbers can be 6 and 10 for the 8-stator-pole WFDSM-DF to eliminate the detrimental influence of UMFs. Based on the above analysis, the stator/rotor pole combinations that produce UMFs are filtered in Table 1 and impaled on a blue strikeout line (▱). It should be noting the UMFs of 12/9-pole machine is negligible, which will be illustrated in section III.

Consequently, except for 16/14 and 16/18 pole combinations, it can be concluded that the recommendable stator/rotor pole combinations for the four-phase WFDSM-DF are $4N/3N$ and $4N/5N$ from the remaining stator/rotor pole combinations in Table 1. The 16/14 and 16/18-pole DAW-WFDSM-DFs are comprised of double 8/7-pole machines and double 8/9-pole machines, respectively. Apart from the advantages of high the ratio γ, the UMFs is also eliminated. However, for dual armature-winding structure, in the limited outer diameter size, more stator poles will increase the geometric conflict between two sets of armature windings and one set of field winding in each stator slot and decrease the stator slot fill factor to reduce the power density. Therefore, the application prospects of DAW-WFDSM-DFs with multiple stator pole structures are generally limited.

In order to comprehensively evaluate the influence of stator/rotor pole combination on the proposed machine performances in terms of output capability, fault-tolerant capability and UMFs, an evaluation function, namely, a weighted-sum-based design objective function, is carried out and expressed as

$$Y = a\frac{T_e}{T_{e\_r}} + b\frac{\gamma}{\gamma_r} + c\frac{F}{F_r} \tag{6}$$

where Y is the objective function and the larger the Y, the better the machine performance. F is the UMF. T_{e_r},
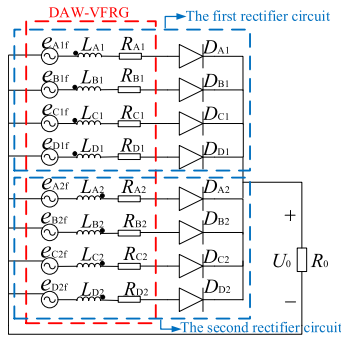
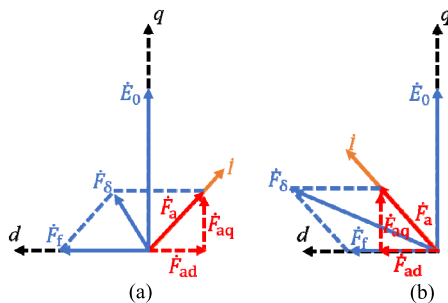**FIGURE 7.** The rectifier topology for four-phase DAW-WFDSM-DF.

FIGURE 8. The simplified phase vector diagrams (a) Demagnetization effect, (b) Enhancing-flux effect (Ff-MMF of field current, Fa- synthetic MMF of four phase current, Fδ-MMF of air gap, I-phase current, E0-phase EMF under no-load, MMF-magnetomotive force, EMF-electromagnetic force).

γ_r and F_r are the reference value. [*a*, *b*, *c*] are the weight factors with larger weight factor indicating a greater importance of the corresponding performance. The sum of these weight factors is 1. In this article, considering that the proposed DAW WFDSM-DF equipped with double-redundant rectifier circuit has potential to improve fault-tolerant capability, therefore, the output capability is considered as the most important indicator, followed by UMFs and finally the fault-tolerant capability. Consequently, the most recommendable stator/rotor pole combinations for the four-phase DAW-WFDSM-DF are $4N/3N$ and $4N/5N$.

B. DOUBLE-REDUNDANT RECTIFIER CIRCUIT

The double-redundant rectifier topology for the four-phase DAW-WFDSM-DF, namely, the hybrid half-wave rectifier (HHWR), is shown in Fig. 7. Two different sets of armature windings in the same phase are required necessarily to form the HHWR. The rectifier circuit types for the two different sets of armature windings in the same phase are different and consequently the armature reactions of the two different sets of armature windings in the same phase are also different. Therefore, the simplified phase vector diagram of DAW-WFDSM-DF is employed in order to clearly illustrated the armature reaction of DAW-WFDSM-DF, as shown in Fig. 8. When the rotor poles slide into the stator poles, the diodes in the first rectifier circuit work, and the armature reaction is a demagnetization effect. The corresponding simplified phase vector diagram is shown in Fig. 8(a). While the rotor poles slide off the stator poles, the diodes in the second rectifier
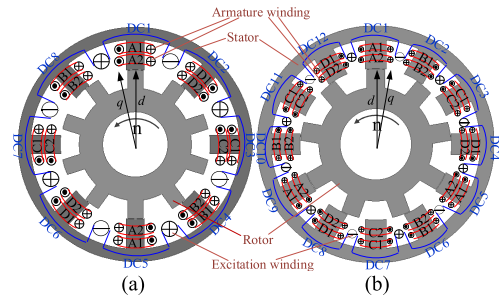

FIGURE 9. Topologies of the four-phase DAW-WFDSM-DF (a) 8/10-pole. (b) 12/9-pole.

circuit work, and the armature reaction is a flux-enhancing effect. The corresponding simplified phase vector diagram is shown in Fig. 8(b). Compared with the demagnetization effect, the phase current under the enhancing-flux effect is larger due to more energy being stored in the magnetic field.

In addition, when the rotor rotates, two sets of parallel rectifier circuits operate simultaneously and back up each other to form a double-redundant drive topology. Therefore, the rectifier topology with double-redundant advantage has the potential to improve the fault-tolerant capability.

III. COMPARATIVE RESEARCH

Based on the above analysis, in order to obtain the better compromise between output capability, UMFs and fault-tolerant capability, the stator/rotor pole combinations for four-phase DAW-WFDSM-DFs with 4N/3N and 4N/5N structures are selected as the comparative research objects. Considering that the fault-tolerant capability of 12/9-pole machine is stronger than that of 8/6-pole one and the output capability of 8/6-pole one is weak, taking 12/9-pole machine and 8/10-pole machine as the representatives of 4N/3N and 4N/5N, respectively. The comparative researches are carried out in detail to determine the optimum topology for four-phase DAW-WFDSM-DF. The corresponding machine topologies are shown in Fig. 9. The first set of armature windings is wound on the bottom of the stator pole, and the second set of armature windings is wound on the top of the stator pole. To simplify the representation, the first set of armature windings of phase A is labelled A1, and the second set of armature windings of phase A is labelled A2. For a fair comparison, both machines are investigated based on the same peripheral dimension, rotating speed, ampere-turn number of the field winding and the rectifier circuit type for two sets of armature windings. The two machines are globally optimized to achieve the maximum output power while constraining the armature current density to 10 A/mm^2 or less due to the limited cooling condition. The main parameters are shown in Table 4.

A. NO-LOAD OPERATIONAL PERFORMANCE

When the field current is 20 A, the no-load flux density and flux line of the four-phase 12/9-pole and 8/10-pole DAW-WFDSM-DFs are shown in Fig. 10. Since the number of ampere-turns of the field winding on each stator pole of the 8/10-pole DAW-WFDSM-DF is bigger than that of

TABLE 4. Parameters of 8/10-Pole and 12/9-Pole Four-Phase DAW-WFDSM-DF.

Parameter	12/9	8/10
Stator outer diameter, D_0 (mm)		180
Stack length, L(mm)		90
Stator pole arc/°	13	14
Rotor pole arc/°	14	12
Air gap (mm)		0.5
Number of turns per coil/ armature windings 1		40
Number of turns per coil/ armature windings 2		40
Number of turns per coil/ field windings	30	45
Slot fill factor		0.55
Rated load R_0 (Ω)	0.5	0.55
Field current I_f(A)		20
Rated speed n (r/min)		1000
Rated output power (kW)		1
Current density of field windings (A/mm²)		8
Current density of armature windings (A/m'm²)	9.2	8.0
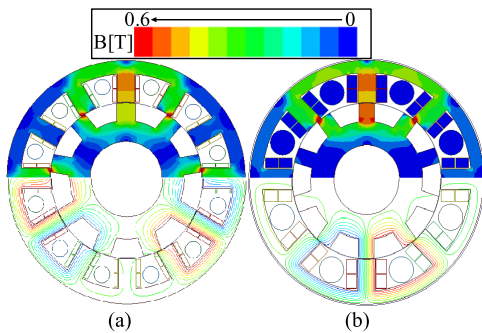
FIGURE 10. The flux density and flux line under no-load (I_f = 20 A, n = 1000 rpm) (a) 12/9-pole. (b) 8/10-pole.
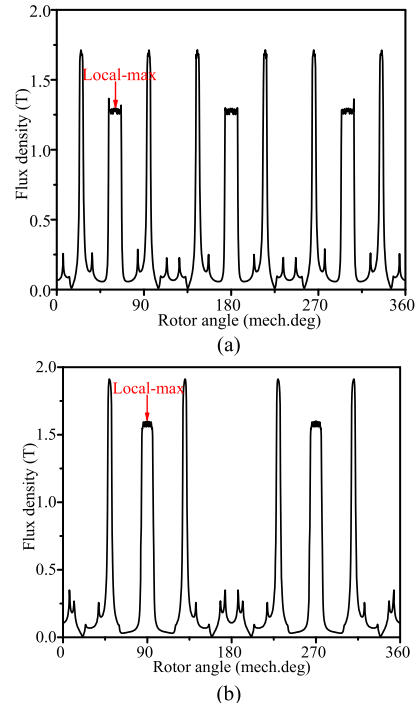

FIGURE 11. Air-gap flux density distributions under no-load (I_f = 20 A, n = 1000 rpm) (a) 12/9-pole. (b) 8/10-pole.
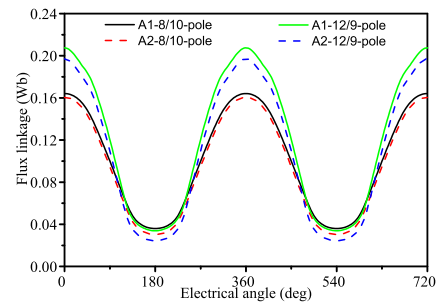

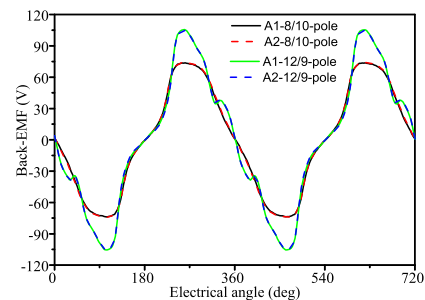**FIGURE 12.** Flux-linkage waveforms under no-load (I_f = 20 A).

FIGURE 13. Phase EMF waveforms under no-load (I_f = 20 A, n = 1000 rpm).

the 12/9-pole one, the magnetic saturation of the 8/10-pole machine is more than that of the 12/9-pole one at the same field current. The no-load air-gap flux density distributions at 1000 rpm are presented in Fig. 11. The local peak values (marked as "Local-max") of the air-gap flux density, namely, the d axial air-gap flux density, are 1.26T and 1.55T for the 12/9-pole machine and 8/10-pole one, respectively. Even if the rotor pole number of the 12/9-pole machine is odd, the UMFs are eliminated due to the circumferentially symmetrical magnetic density in the air gap (see Fig. 11(a)).

The flux-linkage waveforms and phase back-EMF waveforms at 1000 r/min with no-load are presented in Fig. 12 and Fig. 13, respectively. Although the number of armature-turn per phase of the 12/9 machine is 1.5 times than that of the 8/10 one, the maximum flux linkage between the two machines differs by 1.25 times due to the heavier magnetic density of the stator poles for the 8/10-pole machine under aligned conditions. However, the minimum flux linkages of the two machines are approximately equal. The back-EMF under no load can be expressed as follows:

$$E = -W_p W_f I_f \omega \frac{d\lambda}{d\theta} \qquad (7)$$

where W_P and W_f are the turn number of each phase and the turn number of field windings, respectively. The subscript p represents A1, A2, B1, B2, C1, C2, D1 or D2. θ represents the relative position between the stator and rotor poles.

λ is the magnetic permeance of the air gap, and ω is the rotor speed. For either machine, there exists the amplitude difference between the two sets of armature windings in the same phase due to the different flux densities at different positions on the same stator pole. However, the phase back-EMF waveforms of the two sets of armature windings for the same phase are almost the same. It is worth noting that for the 8/10-pole machine and 12/9-pole one, there are some
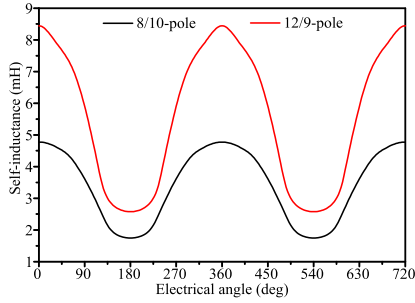
FIGURE 14. A-phase self-inductance waveforms at no-load (I_f = 20 A, n = 1000 rpm).
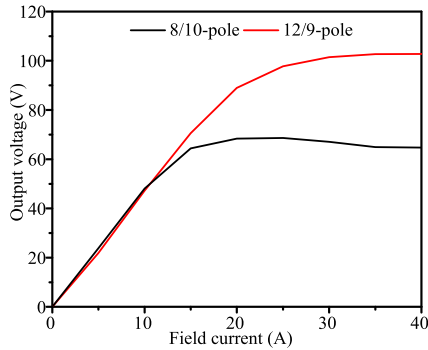

FIGURE 15. Output voltage versus field current under no-load (n = 1000 rpm).

harmonics in the back-EMF waveforms. Since the phases of the coil EMF vectors of the two armature coils making up one phase are the same (see Fig. 2(d)), which causes that all even-order back-EMF harmonics cannot be cancelled in the phase back-EMF and thus there exist some harmonics.

The A-phase self-inductance waveforms with no load are shown in Fig. 14. The self-inductance variation of the 12/9-pole machine is larger than that of the 8/10-pole one, so the flux linkage of the 12/9-pole machine is more easily enhanced or weakened at the same armature current. As the reluctance torque distribution is determined by self-inductance, the output torque ripple of 12/9-pole machine is bigger [20]. The output voltage versus field current is shown in Fig. 15. The flux regulation ability of the 12/9- pole machine is stronger.

B. ON-LOAD OPERATIONAL PERFORMANCE

Fig. 16 shows the external characteristics of output voltage versus load current and output voltage ripple versus load current for both machines when the field current is 20 A and the speed is 1000 rpm. In Fig. 16(a), the output voltage regulation capability of the 12/9-pole machine is stronger than that of the 8/10-pole one. The output voltage ripple can be expressed as follows:

$$U_{0\_ripple} = \frac{U_{0\_max} - U_{0\_min}}{U_{0\_avg}} \qquad (8)$$

In Fig. 16(b), when the load current is smaller than 22 A, the output voltage ripple of the 12/9-pole machine is bigger than that of the 8/10-pole one. When the load current is bigger
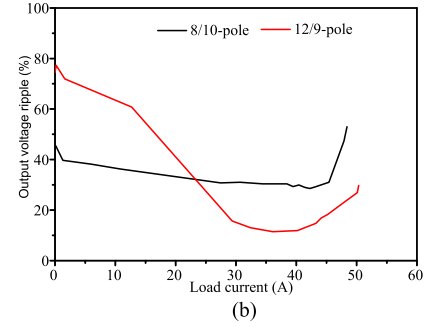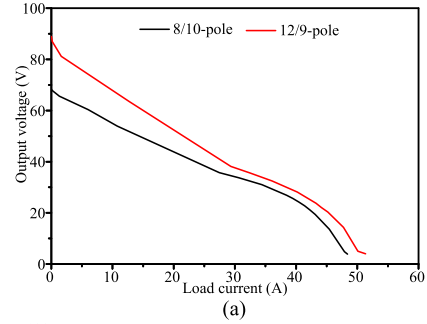

(a)

(b)

FIGURE 16. External characteristics (I_f = 20 A, n = 1000 rpm) (a) output voltage versus load current. (b) output voltage ripple versus load current.
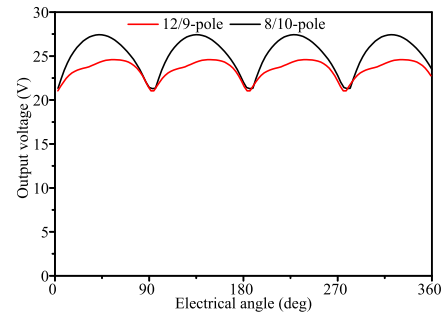

FIGURE 17. Output voltage waveforms at 1 Kw output power (I_f = 20 A, n = 1000 rpm).

than 22 A, the output voltage ripple of the 12/9-pole machine is smaller than that of the 8/10-pole one.

For the two machines, the output power is 1 kW, and the corresponding load resistance values are 0.5 Ω and 0.65 Ω under rated conditions. The corresponding output voltage waveforms without a filter capacitor are shown in Fig. 17.

The output voltages of the 12/9-pole machine and 8/10- pole one are 23.69 V and 24.98 V, respectively. The voltage ripples of the 12/9-pole machine and 8/10-pole one are 14.98% and 24.46%, respectively.

The output power versus rotor speed at the field current of 20 A under rated load is shown in Fig. 18. The powers of both machines are constantly increasing to approach stability as the rotation speed increases. When the speed exceeds 1000 rpm, the power of the 12/9-pole machine is bigger.

Fig. 19 shows the output power versus field current under the rated load when the rotor speed is 1000 rpm. When the field current is greater than 20 A, the power of the 8/10-pole machine tends to be stable since the heavy magnetic saturation. The mutual inductance variation between the field
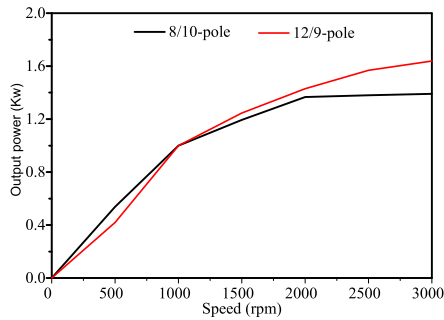
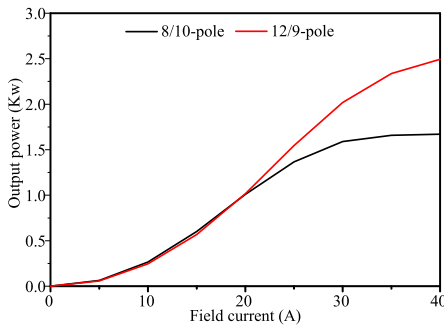**FIGURE 18.** Output power versus rotor speed under rated load (I_f = 20 A).

FIGURE 19. Output power versus field current under rated load (n = 1000 rpm).

FIGURE 20. Core loss versus field current under rated load (n = 1000 rpm).

FIGURE 21. Field current versus speed at 1 kW output power.

winding and armature winding decreases, while the power of the 12/9-pole one continues to increase due to the slight magnetic saturation. Fig. 20 shows the loss variation and efficiency versus field current at the rated load. The armature copper loss of the DAW-WFDSM-DF is computed by:

$$P_{\text{copper}} = 4(I_{\text{rms1}}^2 r_{a1} + I_{\text{rms2}}^2 r_{a2}) \tag{9}$$

where I_{rms1} and I_{rms2} are the rms value of winding current of the first set of armature winding and the second set of one, respectively. r_{a1} and r_{a2} represent the resistance of the set of armature winding and the second set of one, respectively. Besides, the core loss of the DAW-WFDSM-DF core was computed by the FEA software. The magnetic material used in the FEA and prototype is the nonlinear silicon steel DW310-35. Also, the iron loss date is given in [24]. As the field current increases, iron loss increases and then tends to be stable due to heavy core saturation. However, the copper loss always increases with increasing field current. In addition, in the field current range from 5 A to 20 A, the core loss of the 8/10-pole machine is always bigger than that of the 12/9-pole one due to the heavier magnetic saturation of the 8/10-pole one. As the field current increases, the core loss of the 12/9-pole machine exceeds that of the 8/10-pole one. The copper loss of the 12/9-pole machine is always bigger than that of the 8/10-pole one, while the efficiency of the 12/9-pole machine is always less than that of the 8/10-pole one.

Fig. 21 shows the flux weakening capability of the 12/9-pole machine and 8/10-pole one, namely, the field current versus rotor speed at 1 kW of output power. The output power of the 12/9-pole machine and 8/10-pole one remains constant in a speed ra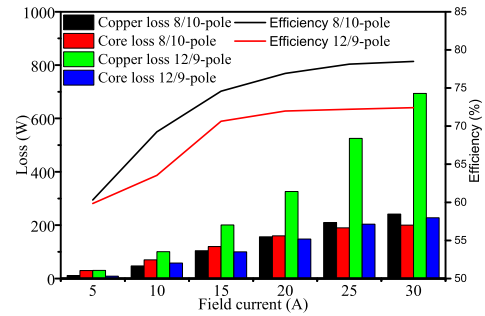nge from 1000 to 3000 rpm by regulating the field current. The flux weakening capability of the 12/9-pole machine is stronger than that of the 8/10-pole one for the same rated output power.

In the proposed 12/9-pole machine and the 8/10-pole one, benefiting from the dual armature winding structure with HHWR, double-redundant effect between two different sets of armature windings is achieved to improve the fault-tolerant capability. Under single winding A1 open-circuit fault condition, the output voltages of both machines are shown Fig. 22. For the 8/10-pole machine, the output voltage under fault condition is 21.85V and is decreased by 12% compared with that under rated condition. Nevertheless, for the 12/9-pole machine, the output voltage under fault condition is 17.92V and is decreased by 24% compared with that under rated condition. What's more, the output voltage ripple of the 12/9-pole machine is more

obvious than that of the 8/10-pole one under the fault condition. Therefore, in terms of single winding open- circuit the fault-tolerant capability of the 8/10-pole machine is stronger than that of the 12/9-pole one.

IV. EXPERIMENTAL VERIFICATION

Compared to the 12/9-pole machines, the copper loss of the 8/10-pole machine is much lower and the efficiency is higher. In addition, because the dual armature winding structure is suitable for low current and high output power applications [12], at a rated power of 1 kW, the output voltage of the 8/10-pole machine is greater than that of the 12/9-pole machine (see Fig. 17). Based on the above analysis, a prototype of four-phase 8/10-pole DAW-WFDSM-DF has been
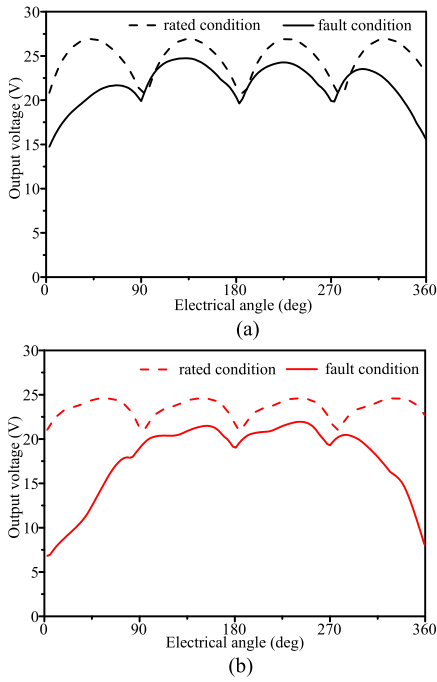
FIGURE 22. Fault-tolerance performance under single winding A1 open-circuit condition (a) 8/10-pole machine. (b) 12/9-pole machine.
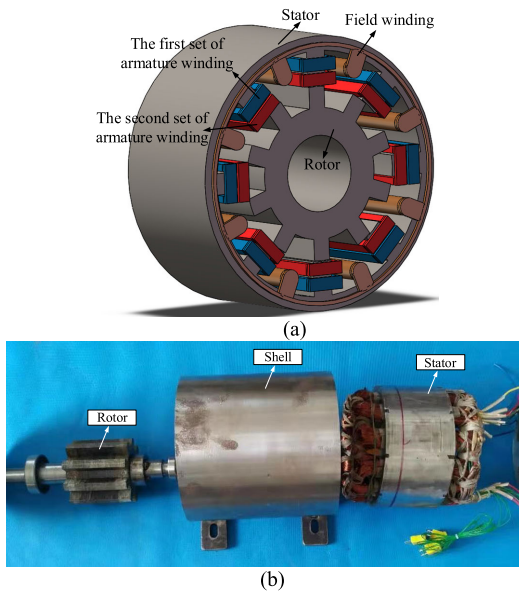

FIGURE 23. Prototype (a) 3D view of the prototype (b) Assembly.

manufactured, and the prototype connected with the hybrid half-bridge rectifier constitutes an 8/10-pole DAW-WFDSM-DF. The 3D view of the 8/10-pole DAW-WFDSM-DF and corresponding assembly are presented in Fig. 23. Benefiting from the concentrated winding connection, the wiring process is simplified and the winding ends are short. The corresponding test rig is shown in Fig. 24.

Fig. 25 shows the measured winding voltage of two different sets of armature windings under no-load. The measured winding voltage amplitudes of the armature winding 1 and the armature winding 2 are both approximately 65V, which agree with the simulation results. The symmetrical winding
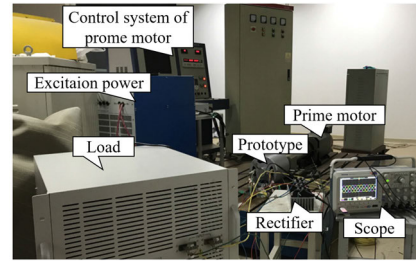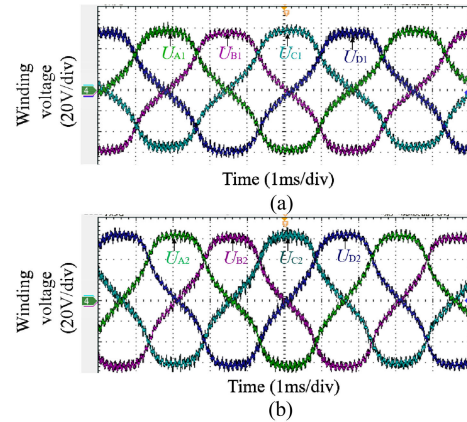

FIGURE 24. Test rig of the prototype.

FIGURE 25. Winding voltage waveforms at no load (n = 1000 rpm, If = 20 A) (a) winding A1, B1, C1 and D1. (b) winding A2, B2, C2 and D2.
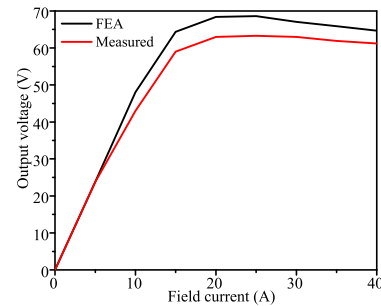

FIGURE 26. Output voltage versus field current at no-load (n = 1000 rpm).

voltage waveforms of each phase winding agree well with the theoretical analysis.

Fig. 26 shows that the simulated and measured waveforms result from the output voltage versus field current under no-load. Due to the neglected end effect in the 2D FE model and the prototype fabrication tolerance, the measured output voltage is slightly lower than the simulated output voltage.

Fig. 27 and Fig. 28 show the measured and simulation winding voltage waveforms and winding current waveforms under rated output power, respectively. The winding voltage including phase back-EMF and armature winding resistance terminal voltage is obtained from FEA, which cause the winding voltage to contain some harmonics, as shown in Fig. 27(c)(d). Due to the armature reaction, the phase voltage waveforms are distorted. What's more, due to the flux-enhancing effect of the armature winding 2, the winding current amplitude is larger compared with the armature
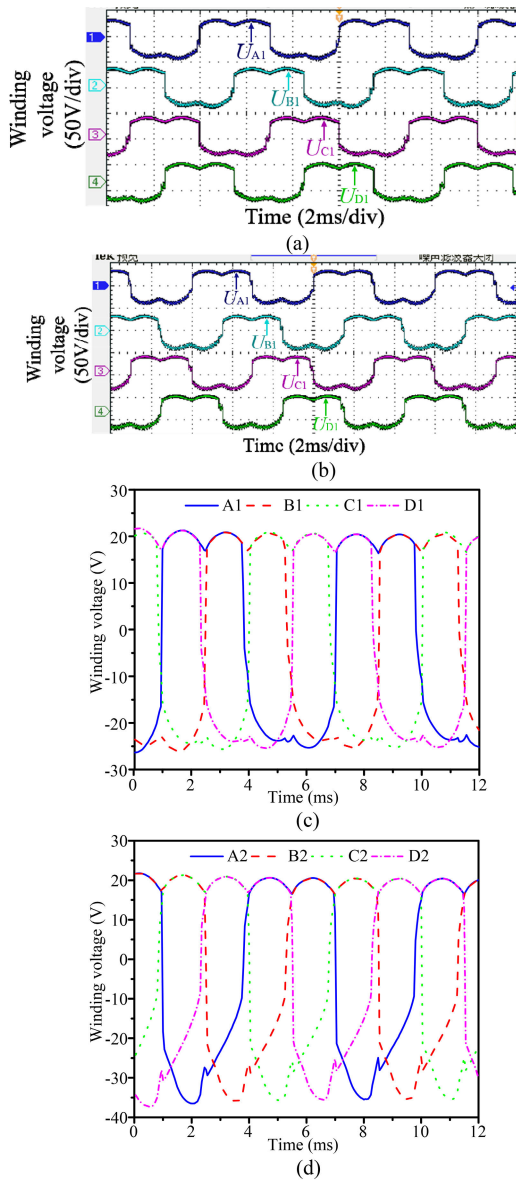
FIGURE 27. Phase voltage waveforms at rated output power (n = 1000 rpm, If = 20 A). (a) Measurement (A1, B1, C1 and D1). (b) Measurement (A2, B2, C2 and D2). (c) Simulation (A1, B1, C1 and D1). (d) Simulation (A2, B2, C2 and D2).

FIGURE 28. Phase current waveforms at on-load (n = 1000 rpm, If = 20 A) (a) Measurement (A1, B1, C1 and D1). (b) Measurement (A2, B2, C2 and D2). (c) Simulation (A1, B1, C1 and D1). (d) Simulation (A2, B2, C2 and D2).

winding 1. In addition, the magnetic densities at the position of the first set of armature windings on the stator poles are heavier compared to that of the second set of armature windings (see Fig. 10(b)), which cause the stronger armature reaction of the first set of armature windings and thus more harmonics in the winding current of the first set of armature windings. Obviously, the simulated waveforms of both winding voltage and winding current agree well with the measured waveforms.

Fig. 29 shows the output voltage versus load current with field currents of 20 A and 1000 rpm by FEA and the experiment. The experimental results are smaller than the FEA results, which resulted from fabrication errors and end effects. Nevertheless, the reliability of the analysis results is still demonstrated.
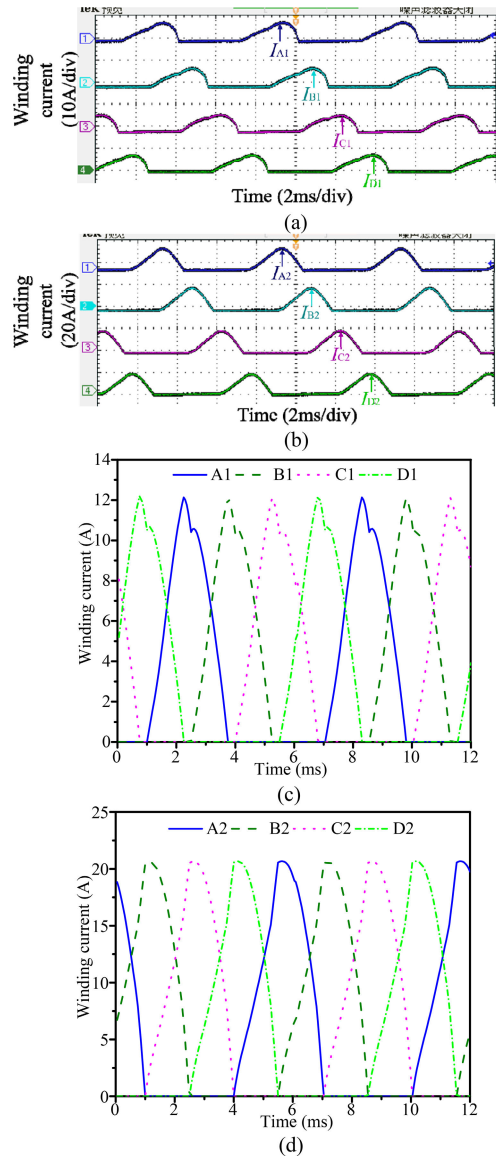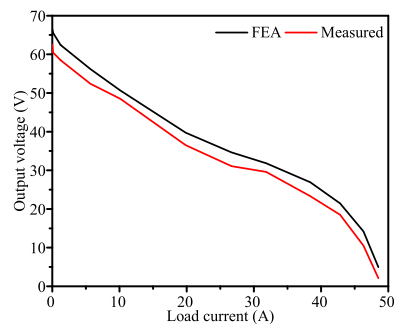

FIGURE 29. Output voltage versus load current (n = 1000 rpm, If = 20 A).

V. CONCLUSION

In this article, a four-phase DAW-WFDSM-DF is proposed to improve the electromagnetic performance including output

voltage ripple, fault-tolerant capability and output capability. The influence of feasible stator/rotor pole combinations on electromagnetic performance is investigated, especially for the fault-tolerant capability. It is found that compared to other combinations, the fault-tolerant capability of the $4N/3N$ and $4N/5N$ combinations is weak due to the low ratio γ. Then, based on a multi-objective evaluation function including output capability, fault-tolerant capability and unbalanced magnetic forces, the $4N/3N$ or $4N/5N$ combinations are most recommended.

In addition, the hybrid half-wave rectifier has the potential of fault-tolerance capability and is introduced in detail.

Then, taking 8/10-pole and 12/9-pole DAW-WFDSG-DFs as the representatives of $4N/5N$ and $4N/3N$, the comprehensive analysis and comparison between the 8/10-pole and 12/9-pole machines with HHWR under no-load

and on-load are presented as follows:

1) The winding configuration in the four-phase machine and dual armature-winding structure with HHWR have promising potential to improve fault-tolerance capability.

2) Due to the circumferentially symmetrical magnetic density in the air gap, the proposed 12/9-pole machine in this article has no significant unbalanced magnetic forces and reduces vibrations and noise.

3) The output voltage and output power regulation capability of the 12/9-pole machine is stronger than that of the 8/10-pole one. The torque ripple of the 8/10-pole machine is smaller than that of the 12/9-pole one due to the smaller self-inductance variation of the 8/10-pole one. The output voltage ripple of the 12/9-pole machine is obviously higher than that of the 8/10-pole one under light load, while the output voltage ripple of the 12/9-pole machine is obviously smaller than that of the 8/10-pole one under heavy load. The 12/9-pole machine exhibits better competitiveness for wide-speed range operation with better output capability.

4) Compared to the 12/9-pole machine, the 8/10-pole one exhibits remarkably higher efficiency under rated conditions and stronger fault-tolerant capability under single winding open-circuit conditions.

Finally, an 8/10-pole prototype is manufactured and tested to verify the analytical results. The simulation and experimental results show that the four-phase DAW-WFDSG-DF with HHWR has promising application prospects in terms of high fault-tolerant capability, low output voltage ripple and low switching loss.

REFERENCES

[1] M. Cheng, W. Hua, J. Zhang, and W. Zhao, "Overview of stator-permanent magnet brushless machines," *IEEE Trans. Ind. Electron.*, vol. 58, no. 11, pp. 5087–5101, Nov. 2011.

[2] X. Zhu, W. Zhao, L. Xu, and J. Ji, "Design and analysis of a new partitioned stator flux-modulation motor for direct drive applications," *IET Electr. Power Appl.*, vol. 14, no. 2, pp. 184–191, Feb. 2020.

[3] S. Wang, S. Niu, and W. Fu, "Comparative study of relieving-DC-saturation hybrid excited Vernier machine with different rotor pole designs for wind power generation," *IEEE Access*, vol. 8, pp. 198900–198911, 2020.

[4] W. Hua, X. Zhu, and Z. Wu, "Influence of coil pitch and stator-slot/rotor-pole combination on back EMF harmonics in flux-reversal permanent magnet machines," *IEEE Trans. Energy Convers.*, vol. 33, no. 3, pp. 1330–1341, Sep. 2018.

[5] X. Zhao, S. Niu, X. Zhang, and W. Fu, "Design of a new Relieving-DC-Saturation hybrid reluctance machine for fault-tolerant in-wheel direct drive," *IEEE Trans. Ind. Electron.*, vol. 67, no. 11, pp. 9571–9581, Nov. 2020.

[6] W. Hua, G. Zhang, and M. Cheng, "Flux-regulation theories and principles of hybrid-excited flux-switching machines," *IEEE Trans. Ind. Electron.*, vol. 62, no. 9, pp. 5359–5369, Sep. 2015.

[7] X. Zhao, S. Niu, X. Zhang, and W. Fu, "A new relieving-DC-saturation hybrid excitation Vernier machine for HEV starter generator application," *IEEE Trans. Ind. Electron.*, vol. 67, no. 8, pp. 6342–6353, Aug. 2020.

[8] L. Sun, Z. Zhang, L. Yu, and X. Gu, "Development and analysis of a new hybrid excitation brushless DC generator with flux modulation effect," *IEEE Trans. Ind. Electron.*, vol. 66, no. 6, pp. 4189–4198, Jun. 2019.

[9] W. Hua, H. Hua, N. Dai, G. Zhao, and M. Cheng, "Comparative study of switched reluctance machines with half-and full-teeth-wound windings," *IEEE Trans. Ind. Electron.*, vol. 63, no. 3, pp. 1414–1424, Mar. 2016.

[10] Z. Zhang, L. Yu, and Y. T. Wang, "Overview and design methodology of doubly salient brushless DC generators with stator-field winding," *IET Electr. Power Appl.*, vol. 11, no. 2, pp. 197–211, 2017.

[11] Z. Chen, H. Wang, and Y. Yan, "A doubly salient starter/generator with two-section twisted-rotor structure for potential future aerospace application," *IEEE Trans. Ind. Electron.*, vol. 59, no. 9, pp. 3588–3595, Sep. 2012.

[12] Y. Zhao, H. Wang, D. Li, and R. Qian, "Comparative research of a wound-field doubly salient generator with different rectifiers," *IEEE Trans. Ind. Informat.*, vol. 14, no. 11, pp. 4851–4863, Nov. 2018.

[13] S. Liwei and Z. Bo, "Analysis of a new five-phase fault-tolerant doubly salient brushless DC generator," *IET Electr. Power Appl.*, vol. 10, no. 7, pp. 633–640, 2016.

[14] L. Yu, Z. Zhang, L. Sun, and Y. Yan, "A split-field-windings doubly salient brushless DC generator with reduced excitation capacity for hybrid electric vehicles," *IEEE Trans. Ind. Electron.*, vol. 65, no. 10, pp. 7697–7708, Oct. 2018.

[15] Y. Xu, Z. Zhang, Z. Bian, and L. Yu, "Copper loss optimization based on bidirectional converter for doubly salient brushless starter/generator system," *IEEE Trans. Ind. Electron.*, early access, Apr. 21, 2020, doi: 10.1109/TIE.2020.2988239.

[16] W. Dai, Y. Yu, M. Hua, and C. Cai, "Voltage regulation system of doubly salient electromagnetic generator based on indirect adaptive fuzzy control," *IEEE Access*, vol. 5, pp. 14187–14194, 2017.

[17] X. Zhou, L. Zhang, and F. Wu, "Operating performance enhancing method for doubly salient electromagnetic machine under light load condition," *IEEE Access*, vol. 8, pp. 112057–112065, 2020.

[18] W. Liu, H. Wang, Y. Wang, L. Xiao, and H. Zhang, "Sensorless control strategy for doubly salient electro-magnetic machine based on the line-to-line excitation flux linkage," *IET Electr. Power Appl.*, vol. 13, no. 12, pp. 1911–1920, 2019.

[19] X. Zhou, B. Zhou, and K. Wang, "Position sensorless control for doubly salient electromagnetic machine with improved startup performance," *IEEE Trans. Ind. Electron.*, vol. 67, no. 3, pp. 1782–1791, Mar. 2020.

[20] L. Sun and Z. Zhang, "Analysis of electromagnetic performance of doubly salient brushless dc generator with distributed field magnetomotive forces," *Proc. CSEE.*, vol. 37, no. 21, pp. 6218–6226, Nov. 2017.

[21] H. Chen, A. M. EL-Refaie, and N. A. O. Demerdash, "Flux-switching permanent magnet machines: A review of opportunities and challenges-Part II: Design aspects, control, and emerging trends," *IEEE Trans. Energy Convers.*, vol. 35, no. 2, pp. 699–713, Jun. 2020.

[22] W. Zhao, L. Xu, and G. Liu, "Overview of permanent-magnet fault-tolerant machines: Topology and design," *CES Trans. Electr. Mach. Syst.*, vol. 2, no. 1, pp. 51–64, Mar. 2018.

[23] Q. Chen, G. Liu, W. Zhao, L. Sun, M. Shao, and Z. Liu, "Design and comparison of two fault-tolerant interior-permanent-magnet motors," *IEEE Trans. Ind. Electron.*, vol. 61, no. 12, pp. 6615–6623, Dec. 2014.

[24] X. Sun, M. Cheng, S. Zhu, and J. Zhang, "Coupled electromagnetic-thermal-mechanical analysis for accurate prediction of dual-mechanical-port machine performance," *IEEE Trans. Ind. Appl.*, vol. 48, no. 6, pp. 2240–2248, Nov. 2012.

YAO ZHAO received the B.S. degree in automation from Anhui University, Hefei, China, in 2009, the M.S. degree in electrical engineering from Shanghai Maritime University, in 2011, and the Ph.D. degree in electrical engineering from the Nanjing University of Aeronautics and Astronautics, in 2016. He is currently a Lecturer with the Shanghai University of Electric Power, China. His current research interests include electrical machines and the power electronization of power systems.

DONGDONG LI (Member, IEEE) was born in Anhui, China, in 1976. He received the B.Sc. degree in electrical engineering from Zhejiang University, in 1998, and the Ph.D. degree in electrical engineering from Shanghai Jiao Tong University, in 2005. From 1998 to 2000, he was with Wuhu power Plant as an Electrical Engineer. He is currently a Professor and the Dean of the School of Electric Engineering, Shanghai University of Electric Power, Shanghai, China. His research interests include the analysis of electric power systems, new energy systems, smart grid, and the power electronization of power systems.

DENGHUI TENG received the B.Eng. degree in electrical engineering from the Zhejiang University of Science and Technology, Hangzhou, China, in 2019. He is currently pursuing the M.S. degree in electrical engineering from the Shanghai University of Electric Power. His research interest includes the design and analysis of doubly salient electric machines.

XING ZHAO (Member, IEEE) received the B.Eng. degree in electrical engineering from the Nanjing University of Aeronautics and Astronautics, China, in 2014, and the Ph.D. degree in electrical engineering from The Hong Kong Polytechnic University, Hong Kong, SAR, in 2020. From July 2019 to January 2020, he was a Research Scholar with the Center for Advanced Power Systems, Florida State University, USA. Since July 2020, he has been with the Department of Electrical Engineering, The Hong Kong Polytechnic University, where he is currently a Research Assistant Professor. He has published more than 25 technical articles in leading journals and six granted patents. His research interests include electrical machines, motor drives, and power electronics for electric propulsion and renewable energy systems. He is an Associate Editor of the IEEE Open Journal of the Industrial Electronics Society.

. . .